Structure of yeast cytochrome *c* oxidase in a supercomplex with cytochrome bc_1

Andrew M. Hartley[1], Natalya Lukoyanova[1], Yunyi Zhang[2], Alfredo Cabrera-Orefice[3], Susanne Arnold[3], Brigitte Meunier[4], Nikos Pinotsis[1*] and Amandine Maréchal[1,2*]

[1] Institute of Structural and Molecular Biology, Birkbeck College, London, U.K.

[2] Institute of Structural and Molecular Biology, University College London, London, U.K.

[3] Radboud Institute for Molecular Life Sciences, Radboud University Medical Center, Nijmegen, The Netherlands.

[4] Institute for Integrative Biology of the Cell, Université Paris-Saclay, Gif-sur-Yvette, France

* e-mail: a.marechal@ucl.ac.uk; n.pinotsis@mail.cryst.bbk.ac.uk

Cytochrome *c* oxidase (complex IV, CIV) is known in mammals to exist independently or in association with other respiratory proteins to form supercomplexes (SCs). In *Saccharomyces cerevisiae*, CIV is found solely in a SC with cytochrome bc_1 (complex III, CIII). Here, we present the cryo-EM structure of *S. cerevisiae* CIV in a III_2IV_2 SC at 3.3 Å resolution. While overall similarity to mammalian homologues is high, we found notable differences in the supernumerary subunits Cox26 and Cox13; the latter exhibits a unique arrangement that precludes CIV dimerization as seen in bovine. A conformational shift in the matrix domain of Cox5A – involved in allosteric inhibition by ATP – may arise from its association with CIII. The CIII–CIV arrangement highlights a conserved interaction interface of CIII, albeit one occupied by complex I in mammalian respirasomes. We discuss our findings in the context of the potential impact of SC formation on CIV regulation.

Introduction

Cytochrome *c* oxidase (or complex IV, CIV) is the last enzyme in the mitochondrial electron transport chain whose activity drives oxidative phosphorylation, the process by which cells produce most of their ATP[1]. CIV is a complex multi-subunit protein embedded in the inner membrane of mitochondria. Its catalytic core, conserved across kingdoms, is composed of three subunits encoded in the mitochondrial DNA. CIV catalyses the reduction of molecular oxygen to water, conserving the released energy as coupled proton transfers across the membrane, through a mechanism that is still highly debated[2]. In addition, mitochondrial forms of CIV have supernumerary subunits (11 in humans), which are encoded in the nuclear genome. The

supernumerary subunits might have a role in CIV assembly or stability, or supercomplex (SC) formation, and there is an increasing interest in understanding the role of specific isoforms in optimising CIV core catalytic function in different tissues or physiological states[3,4].

CIV can exist as a monomer, a dimer, or in a SC with complexes I and/or III in varying stoichiometries ($I–III_2–IV_{1-4}$ and $III_2–IV_{1-2}$) with relative abundances depending on species[5,6] and in mammals, tissue-type, cellular energy requirement and disease state[7-10]. Several structures of complex I-containing SCs have been published recently[11-13] that provide details of their interaction.

Despite its lack of complex I (CI), *Saccharomyces cerevisiae* has been extensively used as a model system for the study of mitochondrial respiratory chains, given its unique genetic amenability[14]. In the case of CIV, *S. cerevisiae* is the only system that contains the supernumerary subunits of so much interest (including isoforms), whilst allowing site-directed mutagenesis of the mitochondrial DNA. This uniquely permits the investigation of fundamental aspects of its catalytic mechanism as well as the identification of putative regulatory elements within supernumerary subunits. In addition, *S. cerevisiae* CIV is known to form SCs with cytochrome bc_1[5] (or complex III, CIII), so it represents an ideal opportunity to investigate the role of SC formation on CIV activity and regulation.

High resolution structural information for the mitochondrial form of the enzyme is limited to crystal structures of dimeric bovine CIV_2[15] and more recently a cryo-EM structure of human CIV[16] within a respirasome. Here, we present the cryo-EM structure of *S. cerevisiae* CIV in a III_2IV_2 SC at 3.3 Å resolution.

Results

Architecture of the III_2IV_2 SC. The III_2IV_2 SC was purified from *S. cerevisiae* mitochondrial membranes after solubilisation with glyco-diosgenin (GDN) and successive metal affinity and gel filtration chromatography (Supplementary Fig. 1). The purified SC is active and reduces molecular oxygen in the presence of exogenous cytochrome *c* at a rate of 30.4 ± 1.3 $e.s^{-1}$ using decylubiquinol as a reductant. When no cytochrome *c* was added, no oxygen reduction was observed (Supplementary Fig. 1).

The cryo-EM map (Table 1) reveals a CIII dimer at the core of the SC flanked by a CIV monomer on either side (Supplementary Fig. 2), as seen in previous low resolution models[17,18]. The core of the map was resolved to <3 Å, but the two CIV monomers could only be resolved to 5–8 Å, consistent with the dynamic nature of CIV within other SC structures[11-13,19]. To address this problem, we used subtracted experimental particle images, focusing only on masked refinements for each CIV monomer as previously described[20]. This procedure increased the resolution of the CIVa and CIVb monomers to 3.31 and 3.38 Å, respectively, revealing new atomic details (Supplementary Fig. 2 and Table 1). The improvement in resolution confirms that the two CIV monomers in the III_2IV_2 SC are identical.

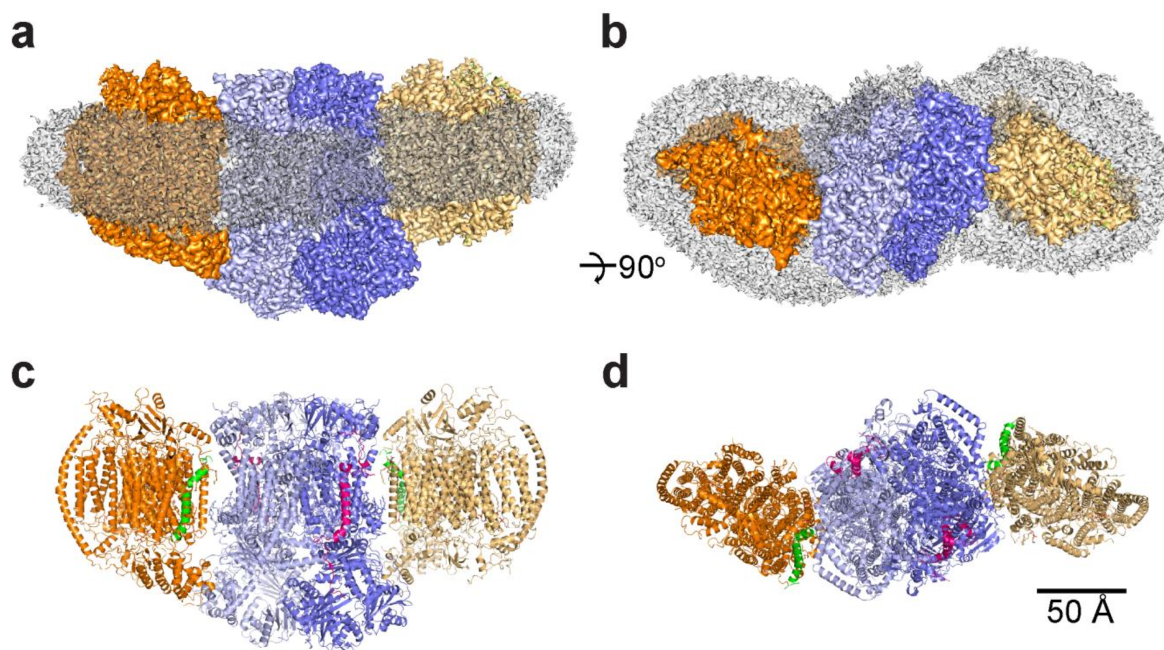

Fig. 1 | Overall structure of the *S. cerevisiae* III_2IV_2 supercomplex.

a, Side and top view of the III_2IV_2 supercomplex (SC) merged cryo-EM map with overall SC dimensions of 289x157x114 Å. CIII and CIV are represented in blue and orange, each monomer being represented by a different shade. The transparent grey density displays the extent of the GDN detergent belt. **b**, Side and top view of the III_2IV_2 SC model. CIII and CIV are represented in the same colours as in **a**, with Cox26 (green) and Qcr10 (red) highlighted.

The merged map (Fig. 1) allowed us to build 44 protein subunits for the III_2IV_2 SC, corresponding to all 20 protein subunits of the obligatory CIII dimer, including Qcr10, which is absent from all yeast structures published to date, and 12 protein subunits for each CIV monomer; the 11 classically described subunits[21,22] and the recently assigned Cox26[23,24]. The presence of all polypeptides forming the III_2IV_2 SC was confirmed by mass spectrometry analyses (Supplementary Table 1). Mass spectrometry also revealed the presence of the respiratory supercomplex factors Rcf1 and Rcf2 in the final protein preparation, but those proteins are absent from the cryo-EM structure. This observation supports the role of Rcf1 and Rcf2 in yeast SC formation[25] but suggests that they are not essential for SC stability, which is similar to findings in mammalian systems. The high resolution of the map allowed the

confident modelling of 96% of all amino acids in the structure (Table 1). All prosthetic groups and metal cofactors are well defined, and 44 lipids including 8 cardiolipin molecules can be confidently modelled.

Atomic resolution structure of the *S. cerevisae* CIV. The yeast CIV structure comprises 12 subunits (Fig. 2a, Supplementary Table 1). Cox1-3 form the catalytic core and are surrounded by 9 supernumerary subunits (Cox4-9, Cox12, Cox13, Cox26). The structure of yeast CIV is remarkably similar to mammalian systems, with a calculated RMSD against bovine[26] and human[16] enzymes of 0.95 and 1.10 Å, respectively, but there are notable differences as discussed below. Subunit composition is also very similar: all but one *S. cerevisiae* subunit (Cox26) have homologues in mammals and conversely, all mammalian subunits but three (COX7B, COX8 and NDUFA4) have yeast homologues. Yeast Cox5 (homologous to mammalian COX4) exists as one of two isoforms depending on oxygen level[27]. In normoxic conditions, almost all CIV is assembled with the Cox5A isoform, although low levels of Cox5B are also expressed. To enhance the homogeneity of our protein preparations, we used a *COX5B* knockout mutant strain (*ΔCOX5B*) that only expresses the Cox5A isoform.

Cox1 and Cox2 house the prosthetic groups responsible for electron transfer and O_2 reduction, namely the dinuclear Cu_A centre, haem *a*, haem a_3 and Cu_B. All prosthetic groups are well resolved in the EM map, as well as the characteristic HPEVY ring of amino acids formed by covalent linkage between $N\varepsilon_2$-His241 and Cε-Tyr245 in Cox1 (Supplementary Fig. 3). Clear densities were observed at the expected magnesium and calcium/sodium binding sites in Cox1 (modelled as a Ca^{2+}

ion[28]) and the zinc binding site in Cox4. The density map also confirms the predicted positioning of the residues forming the D-, K- and H-channels described as putative proton pathways in Cox1 of A1-type oxidases[29].

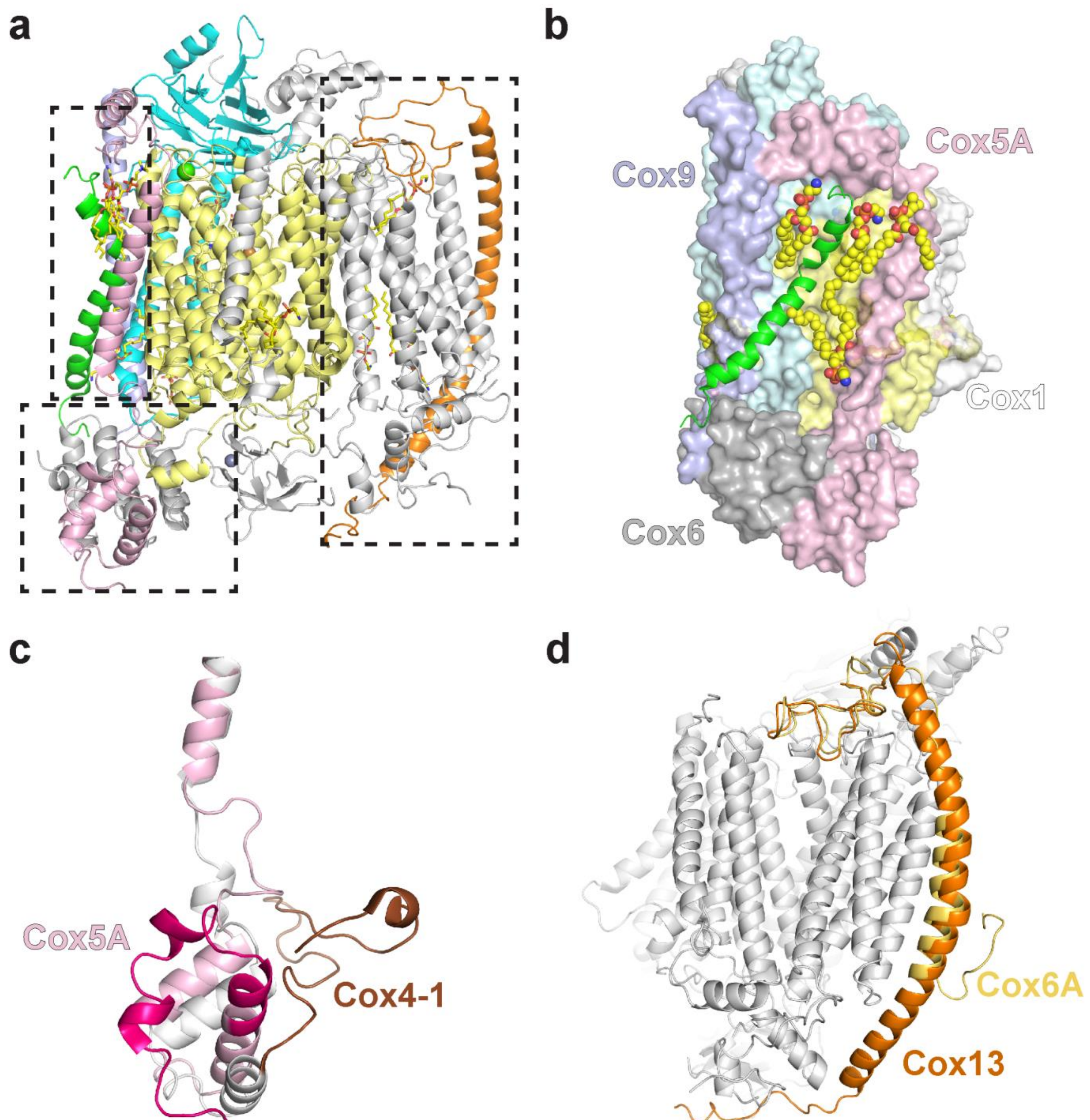

Fig. 2 | Structure of *S. cerevisiae* CIV.

a, Atomic model of CIV showing all 12 subunits. Cox1 is shown in yellow, Cox2 in cyan, Cox5A in pink, Cox26 in green, Cox9 in purple and Cox13 in orange. **b**, Interactions of Cox26 with Cox1, Cox2, Cox6, Cox9 (coloured as in **a**) and lipids (spacefill representation). **c**, Alignment of Cox5A (pink) with its bovine homologue (COX4-1 – grey and brown, PDB 1V54). The first ~50 amino acids are highlighted by

a darker shade. **d**, Differences in length and shape of the transmembrane helix of Cox13 with its bovine homologue (COX6A, PDB 1V54).

Cox26, recently assigned as a subunit of *S. cerevisiae* CIV[23,24], is composed of a single transmembrane helix with a kink towards its C-terminus. This arrangement enables extensive hydrophobic interactions with Cox1 and Cox2 (Fig. 2b), which are further supported by two lipids held against the core of the enzyme. In the matrix, Cox26 interacts at its N-terminus with Cox6 and Cox9 via a network of electrostatic and hydrophobic interactions (Fig. 2b). Deletion of Cox26 does not prevent CIV assembly, nor does it have any significant effect on its activity[23,24]. However, the position of Cox26 in the SC, and the interactions it makes with the subunits above, suggest Cox26 could stabilise the region of CIV at the interface with CIII, supporting a role in formation or stability of the III_2IV_2 SC, even though no direct connection with CIII is evident from the structure.

A notable difference between yeast and mammalian CIV is the conformation of the N-terminal domain of Cox5A (Fig. 2c) which is shifted towards CIII in the *S. cerevisiae* SC to form protein-protein interactions further described below. This region is implicated in allosteric inhibition of CIV by ATP[30-32] and Ser43, a residue which was shown by mutagenesis to contribute to this allosteric effect[32], is at the interface with CIII. More detailed biochemical analyses will be required to determine whether SC formation has a role in the ATP feedback inhibition mechanism.

Another difference is seen in Cox13, the most peripheral subunit of the SC (Fig. 1c, Fig. 2a,d). Cox13 is characterised by a single extended and bow-shaped transmembrane α-helix, protruding from the membrane into the matrix and the intermembrane space (IMS), with a π bulge between residues Ser55 and Leu60. The

N- and C- termini of Cox13 are oriented towards the core of the complex, interacting with Cox1 and Cox3 on the IMS and Cox4 on the matrix side. Its mammalian homologue, COX6A, has a shorter N-terminus that folds back into the membrane, providing the dimerization interface observed in the bovine crystal structure (Fig. 2d). The relevance of the dimeric state of CIV is still disputed, and refinement of CIV within the human respirasome[16] showed that NDUFA4 would prevent dimerization via COX6A. Yeast does not have a NDUFA4 homologue but the peculiar arrangement of Cox13 observed here in the yeast SC would hinder CIV dimerization via this subunit.

Complete structure of *S. cerevisiae* CIII. In *S. cerevisiae*, each CIII monomer consists of 10 subunits. Cytochrome *b*, cytochrome c_1 and Rip1 form the catalytic core containing two haems B, one haem C and a [2Fe-2S] cluster, respectively. All prosthetic groups are visible in the density map along with a molecule of ubiquinone in two apparent configurations at the Q_i site residing between the two cytochrome *b* subunits (Supplementary Fig. 4, Fig. 3). This is a common feature in structures of CIII of various origins, including yeast, whenever the hydrophobic substrate was not completely extracted from the preparation, and it is due to the higher affinity of ubiquinone to the Qi site as compared to Qo. Apart from the presence of Qcr10 and changes resulting from interactions with CIV (see below), our model is consistent with the CIII structures described previously[33].

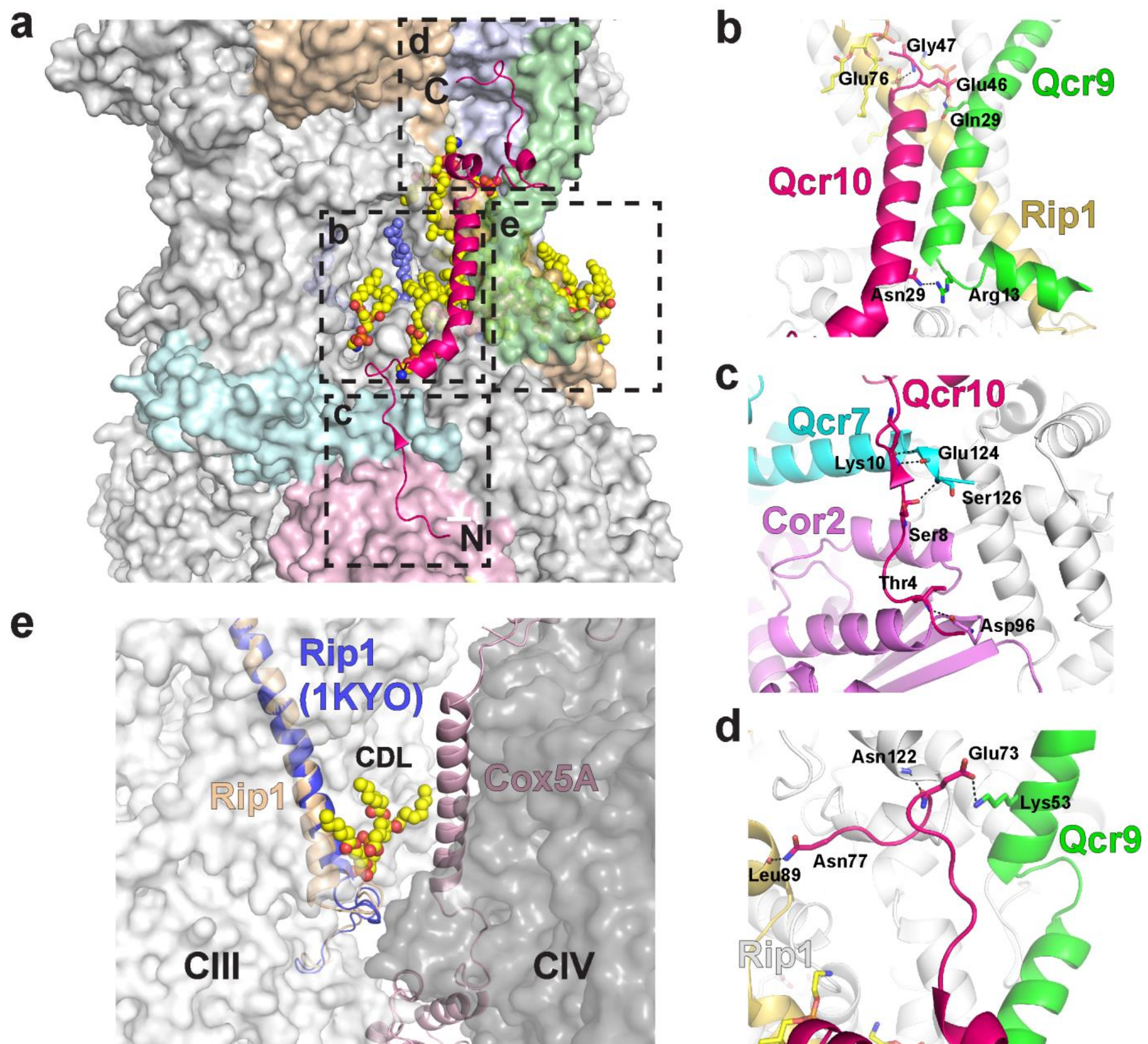

Fig. 3 | Interactions of Qcr10 with other subunits of CIII, and that of Rip1 with a lipid at the interface with CIV.

a, Position of Qcr10 (pink ribbon) in the CIII structure with its N- and C-termini highlighted. Other subunits of CIII that interact with Qcr10 are highlighted in colours. A molecule of ubiquinone at the Qi site is shown as blue spheres. The boxes indicate specific regions of interaction that are highlighted in the other panels. **b**, Qcr10 (pink) forms interactions with the transmembrane helix of Rip1 (yellow) and with Qcr9 (green) at both the matrix and IMS faces of the membrane. **c**, The N-terminal tail of Qcr10 interacts with Cor2 (purple) and Qcr7 (cyan) in the matrix. **d**, Interactions in the IMS between Qcr10 and Cytc_1 (grey), Rip1 (yellow) and Qcr9 (green). **e**, A slight shift in the N-terminus of Rip1 (yellow) compared to the yeast X-ray structure (blue) accommodates interactions with a cardiolipin that goes on to interact with Cox5A of CIV (light pink), forming part of the interface between the two complexes.

Despite low sequence identity, the transmembrane helix of Qcr10 occupies a position similar to that of subunit 11 in mammalian structures[34], making extensive interactions with Qcr9, and with Rip1 on the IMS side of the inner mitochondrial membrane (IMM) supported by a lipid (Fig. 3). In the matrix, the extended N-terminus of Qcr10 interacts with Cor2, and Qcr7 of the other monomer, while in the IMS, Qcr10 extends to interact with cytochrome c_1. These observations are in line with the proposed role of Qcr10 in CIII assembly and Rip1 stability[35].

A conformational change is observed at the N-terminus of the transmembrane helix of Rip1 due to interactions with a cardiolipin molecule that also interacts with Cox5A (Fig. 3 and below) suggesting SC formation could have a role in stabilising this part of CIII. However, this change at the N-terminus does not seem to impact the head domain of Rip1, which maintains its known flexibility.

The CIII-CIV interface. Whilst the CIII dimer is symmetrical and no differences can be seen in the two CIII–CIV interfaces, the alignment of the two halves of the merged SC structure on CIII reveals a deviation of up to 3 Å at the extreme periphery of CIV (Supplementary Fig. 5). This most likely arises from the intrinsic flexibility of the SC and explains why a 3D refinement with C2 symmetry failed to improve the SC resolution (see Methods).

The CIII–CIV interface reveals protein-protein interactions on either side of the IMM, and interactions via bridging lipids in the membrane region itself. The majority of interactions occur on the matrix side between Cor1 and the N-terminus of Cox5A, facilitated by the conformational shift in the latter as described above (Fig. 4a). In the IMS, the C-terminal domain of Cox5A is in position to interact with both the C-

terminus of Qcr6 and a loop region between helices 6 and 7 of cytochrome c_1 (Fig. 4b-c). Within the membrane, Cox5A contacts the N-terminal helix of Rip1 and Qcr8 via a cardiolipin molecule and another lipid modelled as phosphocholine (Fig. 4d). Two other cardiolipins indirectly support the CIII–CIV interface highlighting their crucial role in SC formation[36].

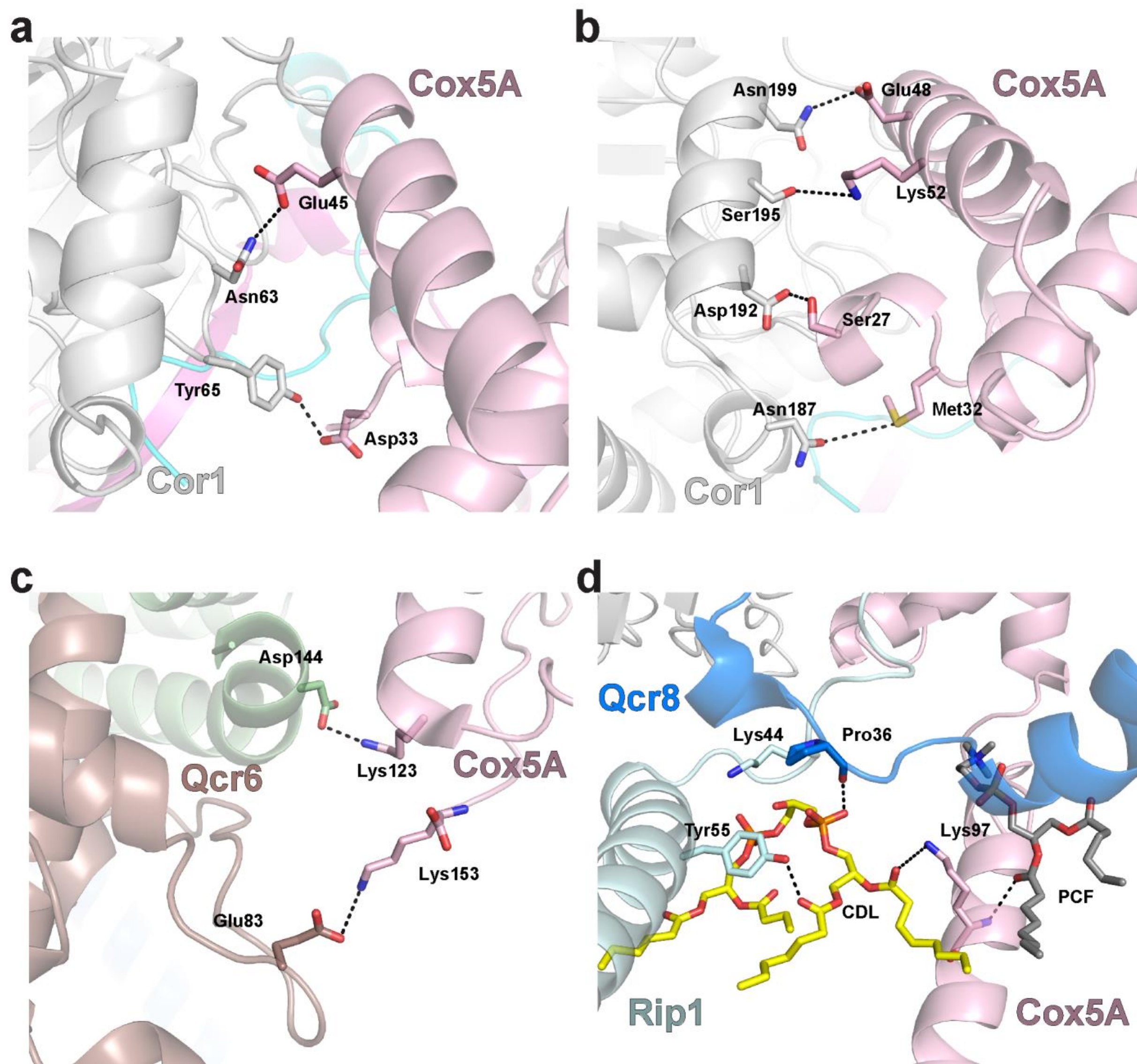

Fig. 4 | Protein-protein interactions between CIV and CIII.

a and **b**, View from the matrix side of protein-protein interactions involving Cor1 (white) and Cox5A (pink). Residues that make inter-subunit interactions are indicated and their interactions are shown as dashed lines. **c**, Interactions between cytochrome c_1 (Cytc_1, brown) and Qcr6 (pale green) with Cox5A (pink) in the IMS. **d**,

A cardiolipin molecule (CDL, yellow) and a phosphocholine (PCF, grey) within the membrane interacts with residues of Cox5A (pink), Rip1 (pale blue) and Qcr8 (blue).

Previous work indicates that mammalian COX7A2L is required for the formation and stability of the CIII–CIV SC in mammals[37] which is consistent with published respirasome structures[11,12]. *S. cerevisiae* has no homologue of COX7A2L so it must follow a different mechanism of CIII–CIV SC formation than the one proposed in mammals. In addition, our work suggests that the III_2IV_2 SC in yeast doesn't require any other proteins to maintain its stability, the interaction between Cox5A and Cor1, two highly conserved subunits, and phospholipids being sufficient to stabilise the SC. However, no mammalian structure of the $III_2IV_{1/2}$ SC is currently available, and in the absence of CI, it cannot be excluded that the CIII–CIV interface is different in a $III_2IV_{1/2}$ supercomplex compared to the respirasome. Mammalian CIV has an additional subunit, COX7B, in front of COX4-1 (the mammalian homolog of Cox5A). However, superimposition of the bovine CIV structure onto the yeast III_2IV_2 SC suggests a similar interaction between CIII and CIV as the one observed in yeast remains possible (Supplementary Fig. 6).

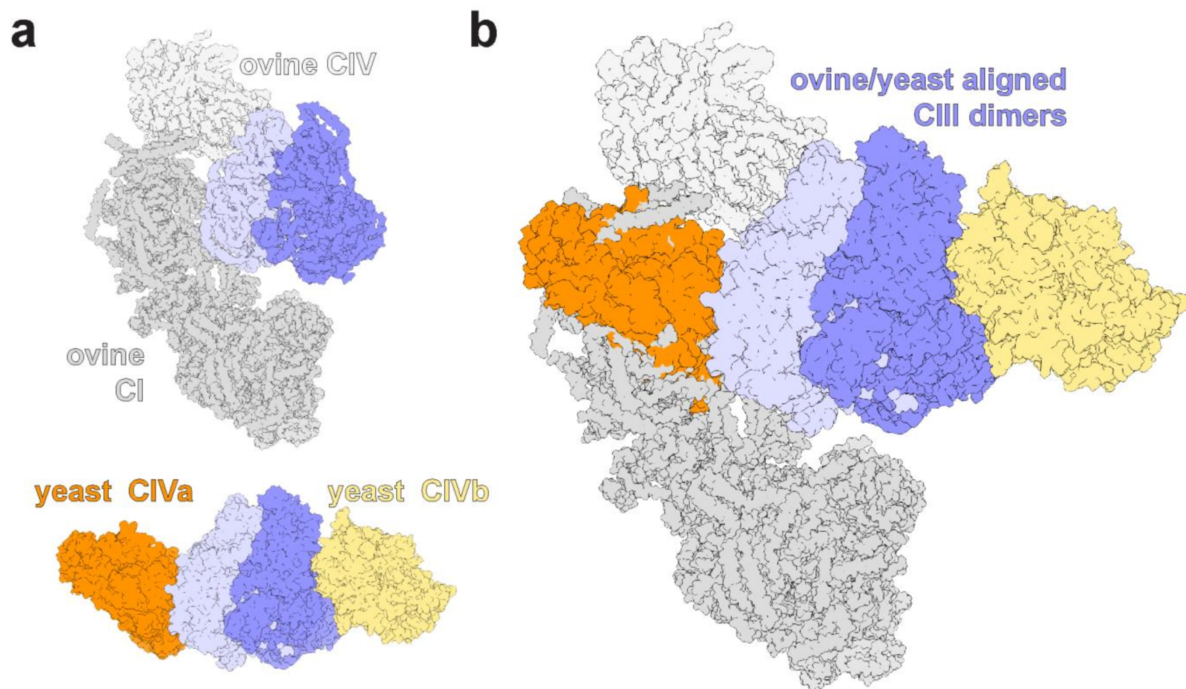

Fig. 5 | Alignment of the mammalian $I_1III_2IV_1$ respirasome with the III_2IV_2 SC from *S. cerevisiae*.

a, The structures of the tight ovine $I_1III_2IV_1$ respirasome[11] (PDB 5J4Z, displayed in shades of grey) and the yeast III_2IV_2 SC (coloured as in Figure 1). **b**, These structures were aligned on their CIII dimers. The view in both **a** and **b** is from the IMS.

Discussion

The functional role of SC formation is still unclear[38,39]. Reactive oxygen species (ROS) prevention by steric inhibition of one half of CIII by CIV in the respirasome has been proposed[40]. In the yeast III_2IV_2 SC, the symmetry of CIII is maintained and no obvious interactions are apparent that could stabilise the hinge region of Rip1, whose flexibility allows the movement of the head group domain, which is implicated in ROS production. However, it is noteworthy that the same subunits of CIII are involved in SC formation in all SC structures resolved so far (Fig. 5). The homologues of yeast CIII subunits Cor1, Rip1, Qcr6 and Qcr8 interact with CI in the

mammalian respirasome structures. These are the same subunits that interact with CIV in our III_2IV_2 structure, highlighting a conservation of the CIII interaction interface, albeit one occupied by CI in mammals and by CIV in *S. cerevisiae,* which lacks CI. Additionally, in the CI-containing *Y. lipolytica* respirasome, where the CIII symmetry is apparently maintained, the suggested CIII–CIV arrangement is similar to the one observed in the yeast III_2IV_2 SC[6]. This suggests that SC formation may serve to stabilise the active CIII monomer(s) by other proteins.

Finally, modulation of CIV activity in response to energy requirements by differential expression of isoforms such as Cox5 in yeast[41] (COX4 in mammals[4]) and COX7A in mammals[42] has been recognised. From the yeast structure presented here, and that of mammalian respirasomes, it seems that these subunits form a substantial part of the interface between proteins in SCs. Therefore, biochemical and biophysical studies investigating these isoforms, and the effect of allosteric sites identified within supernumerary subunits on CIV core catalytic subunits, must take into account SC formation. With homologues of many mammalian supernumerary subunits, extensive genetic amenability and in light of the SC structures now available, *S. cerevisiae* offers a powerful system to study how these factors modulate CIV activity and respiratory SC formation.

Acknowledgements

We would like to thank Diamond Light Source for access and support to the cryo-EM facilities at the UK National electron bio-imaging centre (eBIC, proposal EM14704-36) funded by the Wellcome Trust, the Medical Research Council UK and the Biotechnology and Biological Sciences Research Council. We would also like to thank D. Houldershaw and the computer support group at Birkbeck. This work was supported by the Medical Research Council UK (Career Development Award

MR/M00936X/1 to AM), the Birkbeck Wellcome Trust Institutional Strategic Support Fund (105628/Z/14/Z to AM) and a Wellcome Trust grant to the Birkbeck EM facility (079605/2/06/2).

Author contributions

A.M. designed and supervised the research. B.M. produced the yeast mutant strain. A.M.H. did all the protein work with contribution from Y.Z. A.C.-O. and S.A. performed mass spectrometry analysis. N.L. and A.M.H. performed all microscopy work. A.M.H. and N.P. processed the cryo-EM images. N.P. built the model with inputs from A.M. and A.M.H. A.M., A.M.H. and N.P. wrote the manuscript with contributions from all authors.

Competing interests

The authors declare no competing interests.

References

1. Rich, P. R. & Maréchal, A. The mitochondrial respiratory chain. *Essays Biochem.* **47**, 1-23 (2010).
2. Rich, P. R. Mitochondrial cytochrome *c* oxidase: catalysis, coupling and controversies. *Essays Biochem.* **47**, 1-23 (2010).
3. Pierron, D. *et al.* Cytochrome *c* oxidase: evolution of control via nuclear subunit addition. *Biochim. Biophys. Acta.* **1817**, 590-597 (2012).
4. Horvat, S., Beyer, C & Arnold, S. Effect of hypoxia on the transcription pattern of subunit isoforms and the kinetics of cytochrome *c* oxidase in cortical astrocytes and cerebellar neurons. *J. Neurochem.* **99**, 937-951 (2006).
5. Schägger H. & Pfeiffer, K. Supercomplexes in the respiratory chains of yeast and mammalian mitochondria. *EMBO J.* **19**, 1773-1783 (2000).
6. Davies, K. M., Blum, T. B. & Kühlbrandt, W. Conserved in situ arrangement of complex I and III_2 in mitochondrial respiratory chain supercomplexes of mammals, yeast, and plants. *Proc. Natl. Acad. Sci. USA* **115**, 3024-3029 (2018).
7. Schägger, H. & Pfeiffer, K. The ratio of oxidative phosphorylation complexes I-V in Bovine Heart Mitochondria and the Composition of Respiratory Chain Supercomplexes. *J. Biol. Chem.* **276**, 37861-37867 (2001).
8. Acín-Pérez, R. *et al.* Respiratory active mitochondrial supercomplexes. *Mol. Cell* **32**, 529-539 (2008).
9. Greggio, C. *et al.* Enhanced respiratory chain supercomplex formation in response to exercise in human skeletal muscle. *Cell Metab.* **25**, 301-311 (2017).
10. McKenzie, M., Lazarou, M., Thorburn, D. R. & Ryan, M. T. Mitochondrial Respiratory Chain Supercomplexes Are Destabilized in Barth Syndrome Patients. *J. Mol. Biol.* **361**, 462-469 (2006).

11. Letts, J. A., Fiedorczuk, K. & Sazanov, L. A. The architecture of respiratory supercomplexes. *Nature* **537**, 644-648 (2016).
12. Gu, J. *et al.* The architecture of the mammalian respirasome. *Nature* **537**, 639-643 (2016).
13. Guo, R. *et al.* Architecture of human mitochondrial respiratory megacomplex $I_2III_2IV_2$. *Cell* **170**, 1247-1257 (2017).
14. Lasserre, J. P. *et al.* Yeast as a system for modeling mitochondrial disease mechanisms and discovering therapies. *Dis. Model Mech.* **8**, 509-526 (2015).
15. Tsukihara, T. *et al.* The whole structure of the 13-subunit oxidized cytochrome *c* oxidase at 2.8 Å. *Science* **272**, 1136-1144 (1996).
16. Zong, S. *et al.* Structure of the intact 14-subunit human cytochrome *c* oxidase. *Cell Res.* **28**, 1026-1034 (2018).
17. Heinemeyer, J., Braun, H.-P., Boekema, E. & Kouril, R. A structural model of the cytochrome *c* reductase/oxidase supercomplex from yeast mitochondria. *J. Biol. Chem.* **282**, 12240-12248 (2007).
18. Mileykovskaya, E. *et al.* Arrangement of the respiratory chain complexes in *Saccharomyces cerevisiae* supercomplex III_2IV_2 revealed by single particle cryo-electron microscopy. *J. Biol. Chem.* **287**, 23095-23103 (2012).
19. Sun, C. *et al.* Structure of the alternative complex III in a supercomplex with cytochrome oxidase. *Nature* **557**, 123-126 (2018).
20. Bai, X. C. *et al.* Sampling the conformational space of the catalytic subunit of human ɣ-Secretase. *Elife* **4**, e11182 (2015).
21. Geier, B. M. *et al.* Kinetic properties and ligand binding of the eleven subunit cytochrome *c* oxidase from *Saccharomyces cerevisiae* isolated with a novel large scale purification method. *Eur. J. Biochem.* **227**, 296-302 (1995).
22. Maréchal, A. *et al.* Yeast cytochrome *c* oxidase: a model system to study mitochondrial forms of the haem-copper oxidase superfamily. *Biochim. Biophys. Acta.* **1817**, 620-628 (2012).
23. Levchenco, M. *et al.* Cox26 is a novel stoichiometric subunit of the yeast cytochrome *c* oxidase. *Biochim. Biophys. Acta* **1863**, 1624-1632 (2016).
24. Strecker, V. *et al.* Supercomplex-associated Cox26 protein binds to cytochrome *c* oxidase. *Biochim. Biophys. Acta* **1863**, 1643-1652 (2016).
25. Strogolova, V. *et al.* Rcf1 and Rcf2, members of the hypoxia-induced gene 1 protein family, are critical components of the mitochondrial cytochrome bc_1-cytochrome *c* oxidase supercomplex. *Mol. Cell Biol.* **32**, 1363-1373 (2012).
26. Tsukihara, T. *et al.* The low-spin heme of cytochrome *c* oxidase as the driving element of the proton-pumping process. *Proc. Natl. Acad. Sci. USA* **100**, 15304-15309 (2003).
27. Burke, P. V. *et al.* Effects of oxygen concentration on the expression of cytochrome *c* and cytochrome *c* oxidase genes in yeast. *J. Biol. Chem.* **272**, 14705-14712 (1997).
28. Maréchal, A., Iwaki, M. & Rich, P. R. Structural changes in cytochrome *c* oxidase induced by binding of sodium and calcium ions: an ATR-FTIR study. *J. Am. Chem. Soc.* **135**, 5802-5807 (2013).
29. Rich, P. R. & Maréchal, A. Functions of the hydrophilic channels in protonmotive cytochrome *c* oxidase. *J. R. Soc. Interface* **10**, 1-14 (2013).
30. Arnold, S. & Kadenbach, B. Cell respiration is controlled by ATP, an allosteric inhibitor of cytochrome *c* oxidase. *Eur. J. Biochem.* **249**, 350-354 (1997).
31. Acín-Pérez, R., Gatti, D. L., Bai, Y. & Manfredi, G. Protein phosphorylation and preventation of cytochrome *c* oxidase inhibition by ATP: coupled mechanisms of energy metabolism regulation. *Cell Metab.* **13**, 712-719 (2011).
32. Hess, K. C. *et al.* A mitochondrial CO_2-adenylyl cyclase-cAMP signalosome controls yeast normoxic cytochrome *c* oxidase activity. *FASEB J.* **28**, 4369-4380 (2014).
33. Hunte, C. *et al.* Structure at 2.3 Å resolution of the cytochrome bc_1 complex from the yeast *Saccharomyces cerevisiae* co-crystallized with antibody Fv fragment. *Structure* **8**, 669-684 (2000).
34. Zhang, Z. *et al.* Electron transfer by domain movement in cytochrome bc_1. *Nature* **392**, 677-684 (1998).
35. Brandt, U., Uribe, S., Schägger, H. & Trumpower, B. L. Isolation and characterization of *QCR10*, the nuclear gene encoding the 8.5-kDa subunit 10 of the *Saccharomyces cerevisiae* cytochrome bc_1 complex. *J. Biol. Chem.* **269**, 12947-12953 (1994).
36. Mileykovskaya, E. & Dowhan, W. Cardiolipin-dependent formation of mitochondrial respiratory supercomplexes. *Chem. Phys. Lipids* **179**, 42-48 (2014).

37. Cogliati, S. *et al.* Mechanism of super-assembly of respiratory complexes III and IV. *Nature* **539**, 579-582 (2016).
38. Milenkovic, D., Blaza, J. N., Larsson, N. G. & Hirst, J. The enigma of the respiratory chain supercomplex. *Cell Metab.* **25**, 765-776 (2017).
39. Fedor, J. G. & Hirst, J. Mitochondrial supercomplexes do not enhance catalysis by quinone channeling. *Cell Metab.* **28**, 525-531 (2018).
40. Letts, J. A. & Sazanov, L. A. Clarifying the supercomplex: the higher-order organization of the mitochondrial electron transport cChain. *Nat. Struct. Mol. Biol.* **24**, 800-808 (2017).
41. Allen, L. A., Zhao, X.-J., Caughey, W. & Poyton, R. O. Isoforms of yeast cytochrome *c* oxidase subunit V affect the binuclear reaction center and alter the kinetics of interaction with the isoforms of yeast cytochrome *c*. *J. Biol. Chem.* **270**, 110-118 (1995).
42. Fukuda, R. *et al.* HIF-1 regulates cytochrome oxidase subunits to optimize efficiency of respiration in hypoxic cells. *Cell* **129**, 111-122 (2007).

Tables

Table 1 | Cryo-EM data collection, refinement and validation statistics

	III_2IV_2 SC (EMD-0262, PDB 6HU9)	CIVa (EMD-0269)	CIVb (EMD-0268)
Data collection and processing			
Magnification	130,000		
Voltage (kV)	300		
Electron exposure ($e^-/Å^2$)	1.645		
Defocus range (μm)	-1.6 to -3.6		
Pixel size (Å)	1.048		
Symmetry imposed	C1		
Initial particle images (no.)	98,968		
Final particle images (no.)	44,915		
Map resolution (Å)	3.31	3.31	3.38
FSC threshold	0.143	0.143	0.143
Map resolution range (Å)	-	-	-
Map sharpening *B* factor ($Å^2$)	-60.26	-69.04	-79.03
Refinement[1]			
Initial model used (PDB code)	1KYO, 1V54		
Model resolution (Å)[2]	3.35		
FSC threshold	0.50		
Model resolution range (Å)	3.35		
Model composition			
Nonhydrogen atoms	63,033		
Protein residues	7,636		
Ligands	69		
B factors ($Å^2$)[3]			
Protein	59.9 (141.4 – 20.7)		
Ligand	54.9 (149.7 – 35.5)		
R.m.s. deviations			
Bond lengths (Å)	0.01		
Bond angles (°)	1.32		
Validation[3]			
MolProbity score	2.32		
Clashscore	5.62		
Poor rotamers (%)	8.49		
Ramachandran plot			
Favored (%)	95.61		
Allowed (%)	4.35		
Disallowed (%)	0.04		

[1.] The model was refined against a map generated by merging the map from the 3D refinement (III_2IV_2 SC) with the two maps generated after particle subtraction and 3D refinement focused on CIVa or CIVb.
[2.] Determined by phenix.mtriage
[3.] Determined by phenix.molprobity (values in parenthesis denote highest and lowest values)

Methods

Yeast strain and cell growth. A Δ*COX5B S. cerevisiae* strain only expressing the Cox5A isoform of CIV (α *ade2 leu2 trp1 ura3 cox5B::KanMx4*) with a six-histidine-tag at the C-terminus of COX13 was constructed from W303-1B[43,44]. Yeast cells were grown in YPGal (1% yeast extract, 2% peptone and 2% galactose) medium at 28˚C in 2 L baffled flasks with shaking at 200 rpm as described in Meunier *et al.*[43]. Cells were harvested in late log phase by centrifugation at 6500 rpm for 5 minutes at 4˚C. Cells were washed by resuspension in 50 mM KPi, pH 7.0, and centrifuged again. Cell pellets were stored at -80˚C until use.

Preparation of mitochondrial membranes. Mitochondrial membranes were prepared essentially as described previously[43]. Briefly, thawed yeast cells were resuspended in 30 mL 650 mM D-mannitol, 50 mM KPi, 5 mM EDTA, pH 7.4 containing 0.1 mM PMSF. Glass beads (425-600 μm diameter) were added and cells were broken by mechanical lysis using a bead-beater cell disruptor. Cell debris was removed by centrifugation at 5600 × *g* for 20 minutes at 4˚C, and the supernatant was centrifuged at 120,000 × *g* for 50 minutes at 4˚C to harvest the mitochondrial membranes. The membranes were then resuspended and homogenised in 50 mM KPi, 100 mM KCl, 10 mM $MgCl_2$, 150 μM $CaCl_2$, 0.1 mM PMSF, pH 7.4, and centrifuged as in the previous step. The pellet was then washed by cycles of resuspension/centrifugation in 50 mM KPi, 2 mM EDTA, 0.1 mM PMSF, pH 7.4, until the measure of the absorbance of the supernatant at 260 nm was below 1. Finally, the membranes were resuspended in a minimal volume of 50 mM HEPES, pH 8.0, and stored at -80˚C until use.

Membrane solubilisation and SC purification. Membranes were diluted in 50 mM HEPES, 150 mM NaCl, 1 mM PMSF, pH 8.0 to a CIII concentration of 45 nM and protein complexes were solubilised for 1 hour on ice by the addition of 1% GDN (glyco-diosgenin, Anatrace). After solubilisation, 350 mM NaCl (to make 500 mM final) and 5 mM imidazole are added. Insoluble material was removed by centrifugation at 120,000 × *g* for 30 minutes at 4˚C. Solubilised proteins were then loaded overnight in a cold room at a flow rate of approx. 0.6 mL/min using a peristaltic pump onto a 5 mL HisTrap HP column (GE Healthcare) previously equilibrated with 2 column volumes (CV) of 50 mM HEPES, 500 mM NaCl, 5 mM imidazole, 0.05% GDN, pH 8.0. After loading, the column was washed with 3 CV of 50 mM HEPES, 500 mM NaCl, 5 mM imidazole, 0.05% GDN, pH 8.0, and then with 5 CV of 50 mM HEPES, 150 mM NaCl, 0.05% GDN, 5 mM imidazole, pH 7.2. Bound proteins were eluted with 50 mM HEPES, 150 mM NaCl, 0.05% GDN, 100 mM imidazole, pH 7.2. The eluted proteins were concentrated by centrifugation using 100 kDa MWCO centrifugal concentrators (GE Healthcare). The resulting sample was then further purified by gel filtration, using an Äkta Pure 25 (GE Healthcare) operated at 4˚C with UV detection at 280 nm and automated fraction collection, by loading on a Superose 6 Increase column (GE Healthcare) equilibrated with 50 mM HEPES, 150 mM KCl, 0.05% GDN, pH 7.2. Fractions containing SCs were pooled and concentrated as above, and reapplied once to the same column.

Analytical methods. Resulting fractions were then concentrated and analysed for haem content and purity using UV-visible difference spectroscopy and BN-PAGE. Final protein concentration was determined by the Pierce BCA protein assay (Thermo Scientific) as per the manufacturer’s protocol.

UV-visible difference spectroscopy. UV-visible difference spectra were recorded between 400 and 700 nm using a home built spectrophotometer. Protein samples were diluted as necessary in 50 mM HEPES, 0.1% UDM, pH 8.0. Spectra were measured from sodium dithionite reduced *minus* oxidised spectra, using absorption coefficients ($\Delta\varepsilon$) of 26 mM^{-1} cm^{-1} (604-621 nm) and 28 mM^{-1} cm^{-1} (562-578 nm) for CIV and CIII respectively.

Gel electrophoresis. Protein samples for BN-PAGE analysis were mixed with BN-PAGE sample buffer (final concentration, 50 mM BisTris, 50 mM NaCl, 10% (w/v) glycerol, 0.001% Ponceau S, pH 7.2) as per the manufacturer's instruction (Invitrogen). Pre-cast 3-12% BisTris gels (Novex) were used throughout, and run at 150 V for 90-120 minutes. The running buffer contained 50 mM BisTris, 50 mM Tricine, pH 6.8, and the cathode buffer was made by addition of 0.002% Coomassie G-250 to the running buffer. Gels were destained overnight using 10% (v/v) acetic acid, followed by multiple exchanges of water.

Mass spectroscopy. 50 µg protein of purified III_2IV_2 SC sample were diluted 1:4 in reducing sample buffer consisting of 12% (w/v) SDS, 6% (v/v) β-mercaptoethanol, 30% (w/v) glycerol, 0.05% Coomassie blue G-250 (Serva), 150 mM Tris-HCl pH 7.0 and incubated for 15 min at 37°C. Samples were loaded onto a 10% Tricine-SDS polyacrylamide gel and the electrophoresis was performed according to Schägger[45] until the entire amount of protein entered into the gel (~30 min; 50 V). A molecular mass marker (Precision plus protein standards, dual colour, BioRad) was used to monitor the correct loading of proteins into the gel. Gel-spots containing SC III_2IV_2 were cut and prepared for MS identification, following the in-gel trypsin digestion protocol described previously[46]. Tryptic peptides were separated by liquid chromatography and analysed by tandem mass spectrometry (LC-MS/MS) in a Q-

Exactive 2.0 Orbitrap Mass Spectrometer equipped with an Easy nLC1000 nano-flow ultra-high pressure liquid chromatography system (Thermo Fisher Scientific). MS was run twice for each sample. MS raw data files were analysed using the MaxQuant software (v1.5.0.25) using the settings detailed in Guerrero-Castillo *et al.*[47], except for the search against a compiled version of the *S. cerevisiae* protein database including the pig trypsin and other protein contaminants, such as human keratins.

Activity measurements. Steady-state oxygen consumption rates were measured using a Clark-type oxygen electrode (Oxygraph, Hansatech), operated at 25˚C. Assays were conducted with purified protein at 15 nM, in 10 mM KPi, 50 mM KCl, pH 6.6, supplemented with 0.05% GDN, 500 units/mL SOD and 250 units/mL catalase. SC activity was measured in the presence and absence of 50 µM equine heart cytochrome *c*. The reaction was initiated by addition of 40 µM decylubiquinol. The reaction was stopped by addition of 1 mM KCN and the resulting rate was used as a baseline. Turnover numbers were calculated from linear fitting of the oxygen consumption rate using Origin (OriginLab, Northampton, MA) following the formula T.N. ($e\ s^{-1}$) = O_2 consumption gradient ($M.s^{-1}$) x 4 / [C*c*O] (M). The result presented is the average of four independent experiments (± standard deviation) from two independent protein preparations for cryo-EM.

Cryo-electron microscopy. Purified III_2IV_2 SC (9 mg/mL total protein) was diluted 1:3 in 50 mM HEPES, 150 mM NaCl, 0.05 % GDN, pH 7.2 and applied to glow discharged UltrAuFoil R1.2/1.3 grids (Quantifoil). Grids were blotted for 8.5 seconds at 4˚C and 100% humidity, and then rapidly frozen in liquid ethane using a Vitrobot Mark IV (Thermo Fisher) and stored in liquid nitrogen. Preliminary imaging was done using a Polara microscope operated at 300 kV and equipped with a Quantum energy

filter (Gatan) with a post-GIF K2 Summit direct electron detector (Gatan) operating in counting mode. The primary data were collected using a Titan Krios microscope (Thermo Fisher) operated at 300 kV and equipped with a Quantum energy filter (Gatan) (electron Bio-Imaging Centre, Diamond Light Source, Oxfordshire, UK). The images were collected with a post-GIF K2 Summit direct electron detector (Gatan) operating in counting mode at a nominal magnification of 130,000x, corresponding to the pixel size of 1.048 Å. An energy slit with a width of 20 eV was used during data collection. The dose rate on the specimen was set to 6.58 electrons per $Å^2$ per s and a total dose of 52.64 e/$Å^2$ was fractionated over 32 frames. Data were collected using EPU software (Thermo Fisher) with a nominal defocus range set from -1.6 µm to -3.6 µm. A total of 2740 micrographs were collected.

Image processing. Frame alignment and exposure weighting were performed with MOTIONCOR2[48]. Contrast transfer function parameters of the motion-corrected micrographs were estimated with CTFFIND4.1[49]. Micrographs were screened manually to remove those with excessive specimen drift, overfocus or ice defects. 98,968 particles were selected from the 2634 remaining micrographs using reference-free particle picking with Gautomatch v0.53 (written by Dr Kai Zhang, https://www.mrc-lmb.cam.ac.uk/kzhang/Gautomatch/), using a 360×360 $Å^2$ box size. Particles were sorted using several iterations of reference-free 2D classification in cryoSPARC[50], resulting in a final particle number of 52,257. An initial model was build using *ab-initio* reconstruction in cryoSPARC, which was refined using heterogeneous refinement in RELION v3.0[51]. The III_2IV_2 SC accounted for 44,915 (86%) of the particles present (14% represented the III_2IV_1 supercomplex), and these particles were then used for homogeneous refinement in RELION v3.0 resulting in a 3.31 Å resolution map, based on the FSC-gold standard. Local resolution was

calculated using ResMap[52], revealing a range of resolutions in the map, with the core of CIII resolved to 2.9-3.2 Å, whereas the peripheral edges of the two CIV proteins were resolved to 5-8 Å.

To increase the resolution of the two CIV monomers, we used a particle subtraction approach[20]. In short, a soft mask was generated around III_2IV_b and used to subtract density from the particles, resulting in a new set of particles which was used for focussed 3D refinement of CIVa. This process was repeated with a soft mask around III_2IV_a to refine CIVb. This resulted in an increased resolution of the two CIV monomers to 3.31 Å and 3.38 Å, with a homogeneous distribution of resolution throughout the protein (Supplementary Fig. 2). The two CIV maps were then aligned to the original map of the SC and a merged map was generated using UCSF Chimera[53].

Model building. The three individual maps described above were used for all model building using real space refinement (Table 1) in Coot[54]. A high resolution crystal structure of dimeric CIII (PDB 1KYO)[55], and a yeast homology model[22] were used as starting references for model building. All maps displayed clearly interpretable features such as bulky side chains, metal clusters, haem ligands, cardiolipin and ubiquinone. These features enabled unambiguous assignment of amino-acids in all chains, except some flexible N- and C-termini. Notably, the C-terminus of Rip1 of CIII has weak density (residues 95-215), and this is attributed to its characteristic flexibility. Its Fe-S cluster is clearly visible in the map. Finally, the N-terminal residues of Qcr6 (1-73) in CIII, are not resolved, a feature common to all yeast CIII crystal structures, possibly due to the high composition of charged residues in this region. Additional densities in the map indicated the presence of long carbon chains which were modelled as di-palmitoyl-phosphatidylethanolamine

(PEF), diacyl-glycero-phosphocholine (PCF) and cardiolipin (CDL) molecules based on map interpretation and similarities with previous structures where these ligands were found. Lipid tails were truncated according to the density maps. The three models (dimeric CIII, and two CIV monomers) where then individually refined using the real space refine tool in Phenix[56], using secondary structure restraints. Geometry definitions for the ligands were defined from values in the *CCP*4 ligand library[57]. Additional bond and distance restraints were implemented on specific molecules based on previously published high resolution structures. For initial refinement in Phenix, Ramachandran and rotamer constraints were also used. The models were then visually inspected in Coot for additional corrections. A final real space refinement was performed in Phenix by disabling rotamer constrains resulting in an increase of the model-to-map fit. To confirm the validity of the map, a final real space refinement was performed to the complete III_2IV_2 SC using the merged map described above. The final model contains 7,636 protein residues and 69 ligands. For the CIII dimer we modelled four B-haems and one ubiquinone molecule in the two cytochrome *b* subunits, one C-haem for each cytochrome c_1 subunit, one [2Fe-2S] iron-sulphur cluster for each Rip1 subunit, eight cardiolipin molecules, twelve PEF and six PCF molecules. For each CIV we modelled a haem *a*, haem a_3 and Cu_B in Cox1 as well as one calcium and one magnesium ions. In Cox2 we modelled a dinuclear Cu_A centre and in Cox4 one zinc ion. Each CIV contains additionally eight PEF molecules and one PCF molecule. Refinement and model statistics are summarized in Table 1. Map and molecule representations in the figures were prepared by PyMOL (https://pymol.org/) and UCSF Chimera.

Data availability

All relevant data are included in the manuscript and/or are available from the corresponding authors upon reasonable request. Cryo-EM maps have been deposited in the Electron Microscopy Data Bank (EMDB) under accession codes EMD-0262 (III_2IV_2 SC), EMD-0269 (CIVa), EMD-0268 (CIVb). The coordinates of the atomic model of the III_2IV_2 SC built from a combination of the three maps have been deposited in the Protein Data Bank (PDB) under accession code 6HU9.

References

43. Meunier, B., Maréchal, A. and Rich, P. R. Construction of histidine-tagged yeast mitochondrial cytochrome *c* oxidase for facile purification of mutant forms. *Biochem. J.* **444**, 199-204 (2012).
44. Dodia, R., Meunier, B., Kay, C. W. M. & Rich, P. R. Comparisons of subunit 5A and 5B isozymes of yeast cytochrome *c* oxidase. *Biochem. J.* **464**, 335-342 (2014).
45. Schägger, H. Tricine-SDS-PAGE. *Nat. Protoc.* **1**, 16-22 (2006).
46. Heide, H. *et al.* Complexome profiling identifies TMEM126B as a component of the mitochondrial complex I assembly complex. *Cell Metab.* **16**, 538-549 (2012).
47. Guerrero-Castillo, S., Cabrera-Orefice, A., Huynen, M. A. & Arnold, S. Identification and evolutionary analysis of tissue-specific isoforms of mitochondrial complex I subunit NDUFV3. *Biochim. Biophys. Acta* **1858**, 208-217 (2017).
48. Zheng, S. Q. *et al.* MotionCor2: anisotropic correction of beam-induced motion for improved cryo-electron microscopy. *Nat. Methods* **14**, 331-332 (2017).
49. Rohou, A. & Grigorieff, N. CTFFIND4: fast and accurate defocus estimation from electron micrographs. *J. Struct. Biol.* **192**, 216-221 (2015).
50. Punjani, A., Rubinstein, J. L., Fleet, D. J. & Brubaker, M. A. CryoSPARC: algorithms for rapid unsupervised cryo-EM structure determination. *Nat. Methods* **14**, 290-296 (2017).
51. Scheres, S. H. RELION: implementation of a Bayesian approach to cryo-EM structure determination. *J. Struct. Biol.* **180**, 519-530 (2012).
52. Kucukelbir, A., Sigworth, F. J. & Tagare, H. D. Quantifying the local resolution of cryo-EM density maps. *Nat. Methods* **11**, 63-65 (2014).
53. Pettersen, E.F. *et al.* UCSF Chimera--a visualization system for exploratory research and analysis. *J. Comput. Chem.* **25**, 1605-1612 (2004).
54. Emsley, P., Lohkamp, B., Scott, W. G. & Cowtan, K. Features and development of Coot. *Acta Crystallogr. D* **66**, 486-501 (2010).
55. Lange, C. & Hunte, C. Crystal structure of the yeast cytochrome bc_1 complex with its bound substrate cytochrome *c*. *Proc. Natl. Acad. Sci. USA* **99**, 2800-2805 (2002).
56. Adams, P. D. *et al.* PHENIX: a comprehensive Python-based system for macromolecular structure solution. *Acta Crystallogr. D* **66**, 213-221 (2010).
57. Winn, M. D. *et al.* Overview of the *CCP*4 suite and current developments. *Acta Crystallogr. D* **67**, 235-242 (2011).

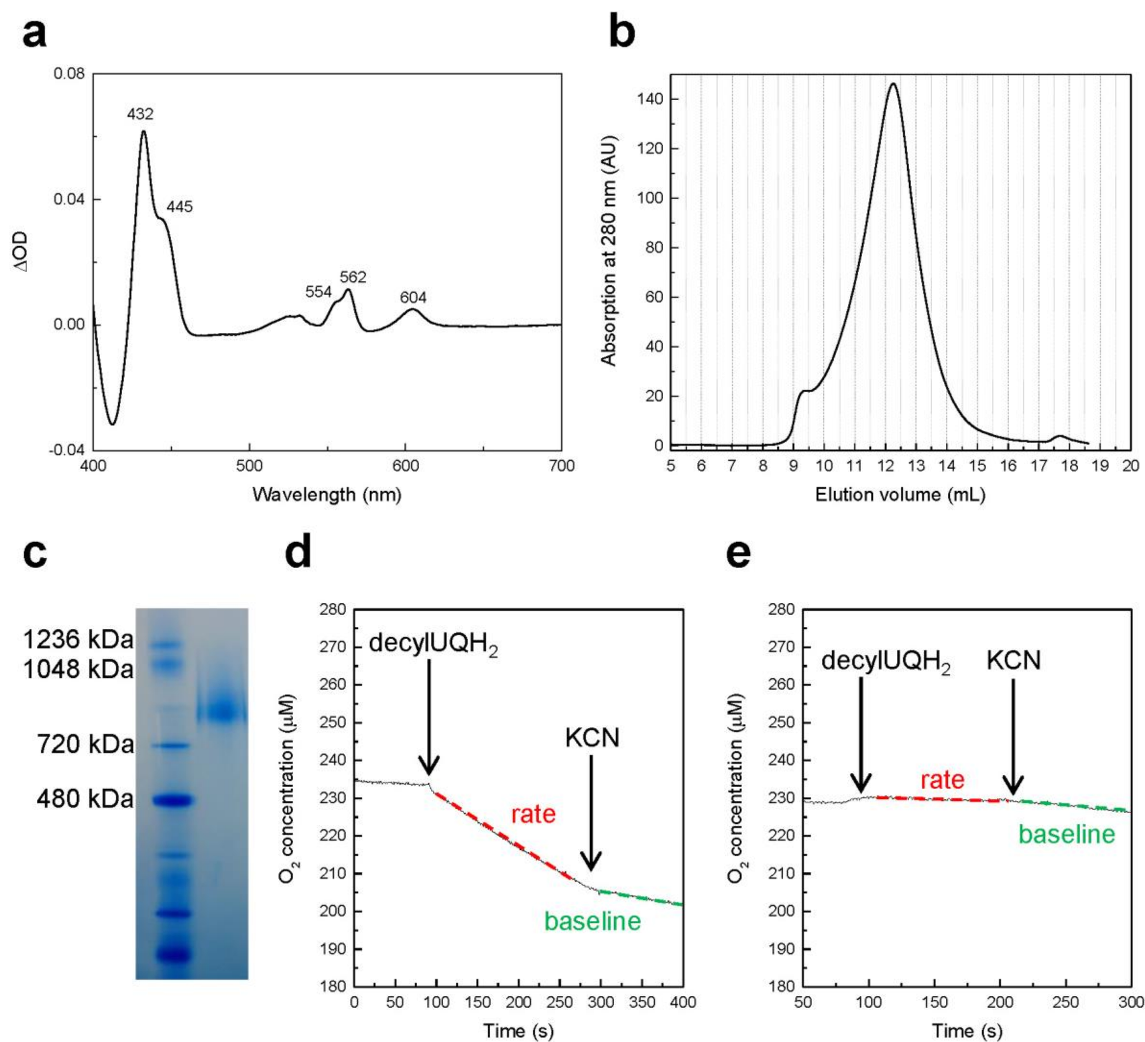

Supplementary Figure 1. Biochemical characterisation of *S. cerevisiae* III_2IV_2 SC.
a, UV-visible redox spectrum of the purified yeast III_2IV_2 SC. Peaks are labelled and correspond to the A-type haems present in CIV (445/604 nm) and the B- and C-type haems present in CIII (432/562 nm and 554 nm). **b**, Gel filtration profile of the yeast III_2IV_2 SC. The fraction eluting between 12-12.5 mL was used for cryo-EM. **c**, BN-PAGE gel of the purified yeast III_2IV_2 SC. **d**, Oxygen consumption rate of the III_2IV_2 SC (red line) in the presence of 50 μM cytochrome *c*, initiated by addition of 40 μM decylubiquinol (decylUQH_2). A baseline (green) is recorded after addition of 1 mM KCN, an inhibitor of CIV. **e**, Oxygen consumption rate of the III_2IV_2 SC without exogenous cytochrome *c* (experiment details are as in **d**). Data in **a**-**c** are representative of three independent experiments with similar results.

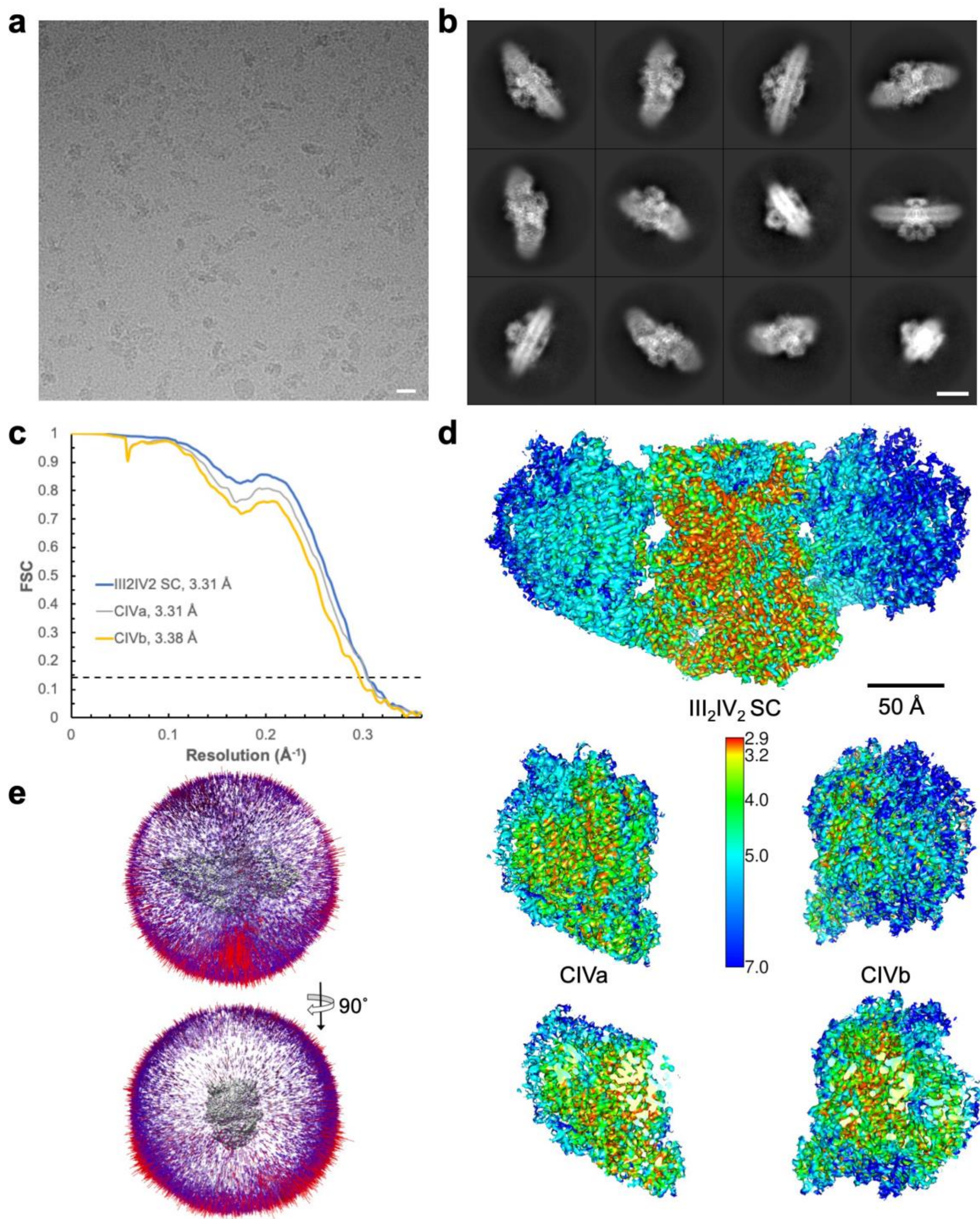

Supplementary Figure 2. Cryo-EM data collection and workflow of 3D classification and focussed refinement.

a, A representative cryo-EM micrograph of III_2IV_2 SC (scale bar, 30 nm). **b**, Representative 2D class averages of the III_2IV_2 SC (scale bar, 20 nm). **c**, Fourier shell correlation (FSC) curves between two independently refined half-maps for the III_2IV_2 SC map, and for the two CIV maps, each individually refined. **d**, Surface rendering maps coloured according to local resolution. Upper and middle present the maps of the III_2IV_2 SC, and CIVa and CIVb after focused refinement. The lower display shows the central sections of the two CIV maps to emphasise further the improvement in resolution (scale bar, 50 Å). **e**, Euler angle distributions of the 44,915 particles included in the calculation of the III_2IV_2 SC map for two orientations rotated by 90 degrees. Data collection and structure calculation were not repeated.

Supplementary Table 2. Mass spectrometry analysis of the subunits present in the yeast III_2IV_2 SC.

Gene name	*Protein name*	*Uniprot entry*	*Precursor M_r*	*Mature M_r*	*Mature protein*	*Peptides identified*		*Sequence coverage*	*IBAQ value*
			kDa	kDa	residues	total	unique	%	x10^6
Cytochrome *c* oxidase									
COX1	Cox1	P00401	58.797	58.797	1-534	5	5	13.9	200
COX2	Cox2	P00410	28.567	26.763	16-251	10	10	53.0	2,368
COX3	Cox3	P00420	30.360	30.360	1-269	1	1	6.3	59
COX4	Cox4	P04037	17.143	14.172	26-155	13	13	85.8	2,017
COX5A	Cox5A	P00424	17.140	14.875	21-153	11	9	42.5	805
COX6	Cox6	P00427	17.341	12.627	41-148	9	9	54.7	1,319
COX7	Cox7	P10174	6.932	6.801	2-60	2	2	20.0	505
COX8	Cox8	P04039	8.907	5.366	28-74	1	1	12.8	261
COX9	Cox9	P07255	6.963	6.461	2-56	7	7	39.0	2,220
COX12	Cox12	Q01519	9.788	9.657	2-83	8	8	81.9	271
COX13	Cox13	P32799	15.021	13.837	10-129	11	11	68.2	651
COX26	Cox26	Q2V2P9	7.452	7.452	1-66	3	3	30.3	1,008
RCF1	Rcf1, AIM31	Q03713	18.477	18.477	1-159	18	18	79.2	352
RCF2	Rcf2, AIM38	P53721	25.344	25.344	1-224	12	12	45.1	921
Cytochrome *bc*$_1$ complex									
COB	cytochrome *b*	P00163	43.656	43.656	1-385	3	3	7.0	1,211
CYT1	cytochrome *c*$_1$	P07143	34.055	27.771	62-309	18	18	59.5	2,995
RIP1	Rip1	P08067	23.365	20.099	31-215	19	19	60.9	2,742
COR1	Cor1	P07256	50.227	47.409	27-457	33	33	76.4	4,107
QCR2	Cor2	P07257	40.478	38.705	17-368	40	40	85.6	4,039
QCR6	Qcr6	P00127	17.257	17.257	1-147	4	4	32.0	1,023
QCR7	Qcr7	P00128	14.565	14.565	1-127	13	13	90.6	3,052
QCR8	Qcr8	P08525	10.974	10.974	1-94	7	7	68.1	1,202
QCR9	Qcr9	P22289	7.476	7.345	2-66	3	3	28.8	1,642
QCR10	Qcr10	P37299	8.593	8.462	2-77	5	5	46.8	587

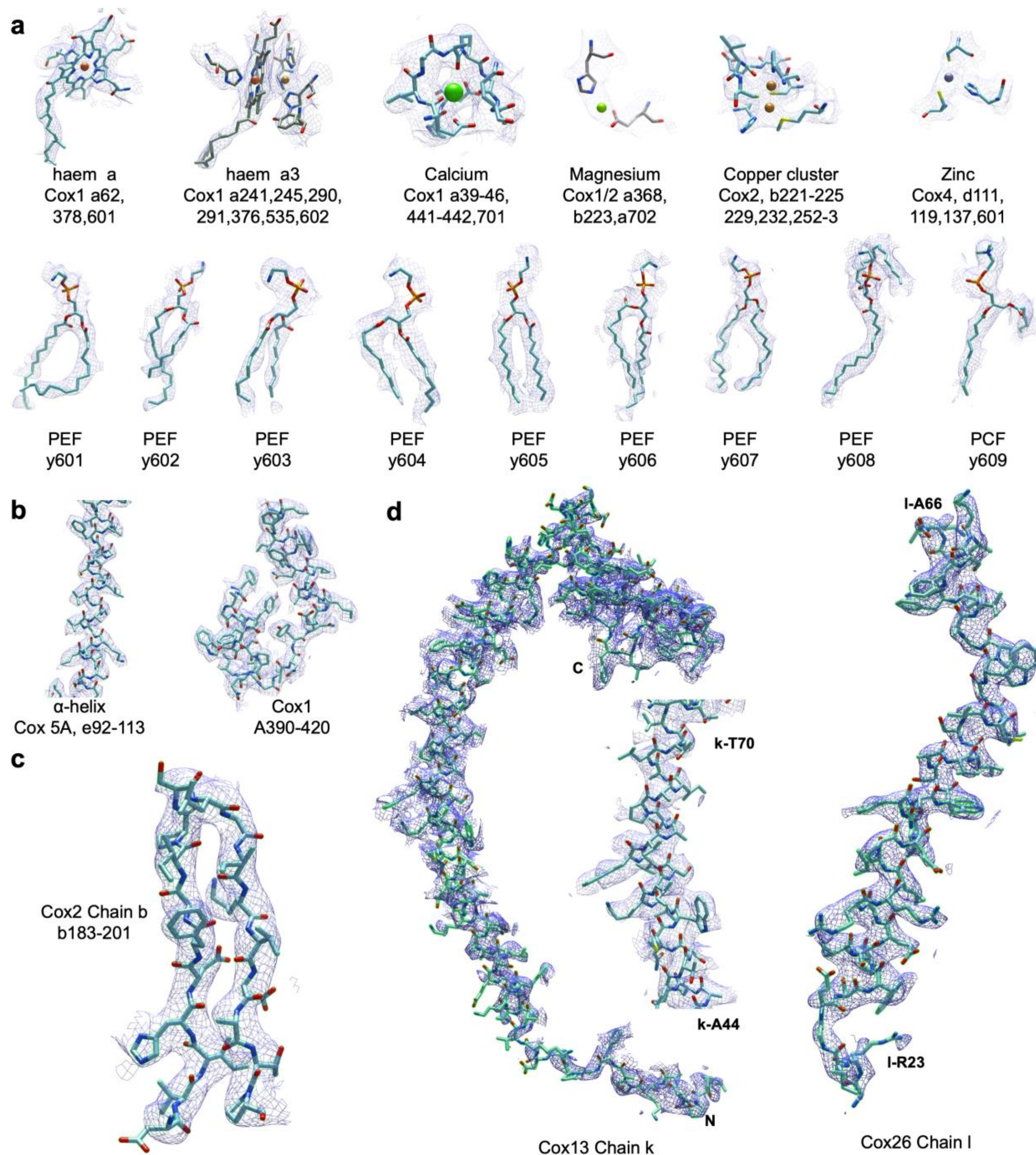

Supplementary Figure 3. Fitting of the CIV model into the cryo-EM density.

a, Fitting of co-factors, metal clusters and identified lipids into the CIVa cryo-EM map density. Below each model are the names of the co-factor/metal/lipid, alongside the domain, and chain as in PDB 6HU9, they belong to. The numbering refers to residues found nearby, or providing coordination (PEF, palmitoyl-phosphatidylethanolamine, PCF, diacyl-glycero-phosphocholine). **b**, Two examples of high resolution α-helical regions of CIV, Cox5A which forms the interface with CIII, and the core domain Cox1. **c**, Fitting of a β-sheet from Cox2. **d**, Fitting of the distal subunit Cox13 (chain k) and the new subunit Cox26 (chain l) into the density. The N- and C-termini of the chains are indicated. The corresponding co-factors, metals, lipids and subunits from the other CIV monomer (CIVb) display identical density (not shown).

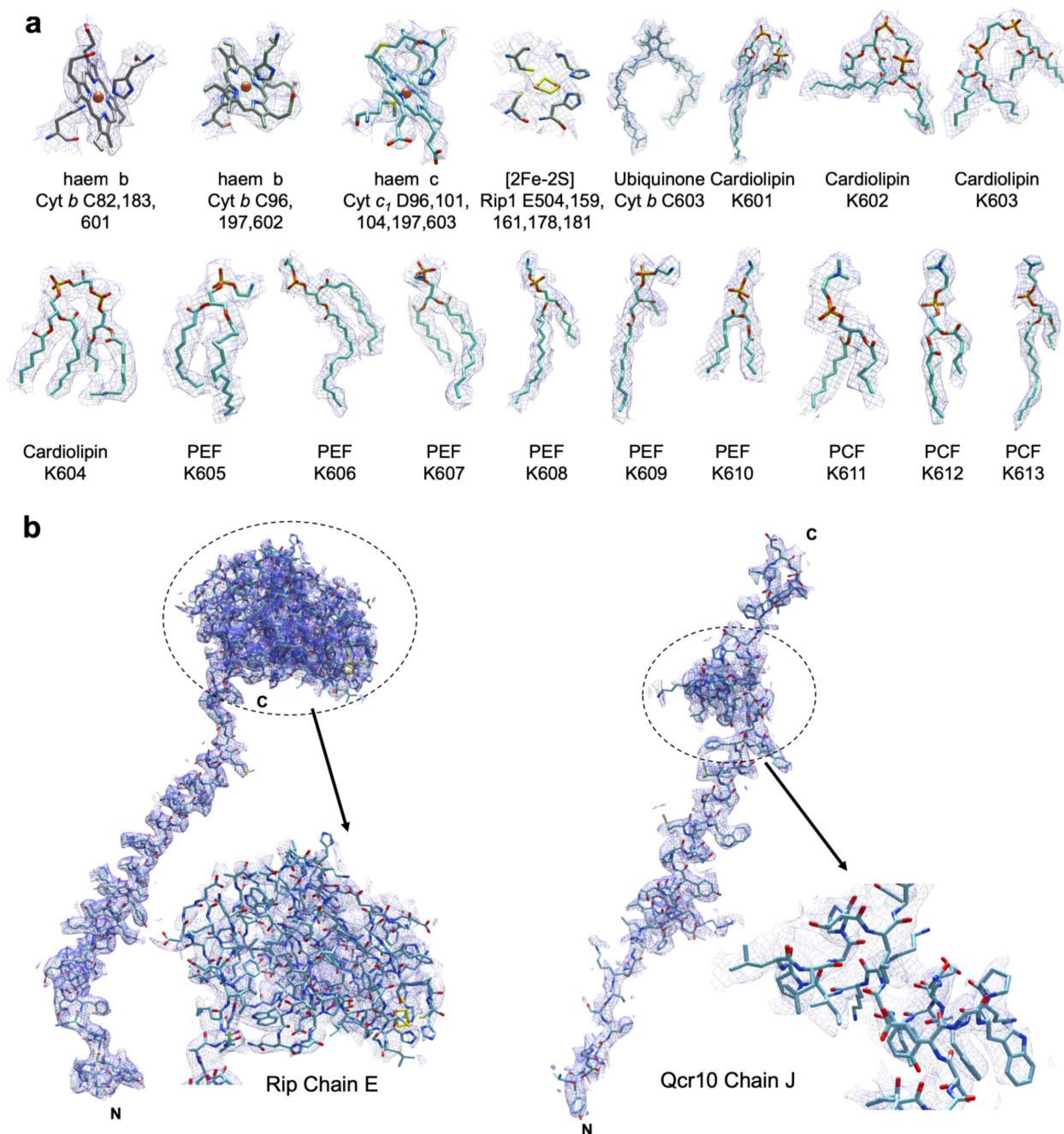

Supplementary Figure 4. Fitting of the CIII model into the cryo-EM density.
a, Fitting of co-factors, metal clusters and identified lipids into the III_2IV_2 SC cryo-EM map density. Below each model are the names of the co-factor/metal/lipid, alongside the domain, and chain as in PDB 6HU9, they belong to. The numbering refers to residues found nearby, or providing coordination (PEF, palmitoyl-phosphatidylethanolamine, PCF, diacyl-glycero-phosphocholine). **b**, Fitting of the subunits Rip1 (chain E) and Qcr10 (chain J) into the density. The N- and C-termini of the chains are indicated. Note the lower resolution of the flexible C-terminal catalytic domain of Rip1 (zoom in). This domain, as well as Qcr10, display higher B-factors compared to the other subunits of CIII (not shown). The corresponding domains from the second monomer of CIII display identical density (not shown).

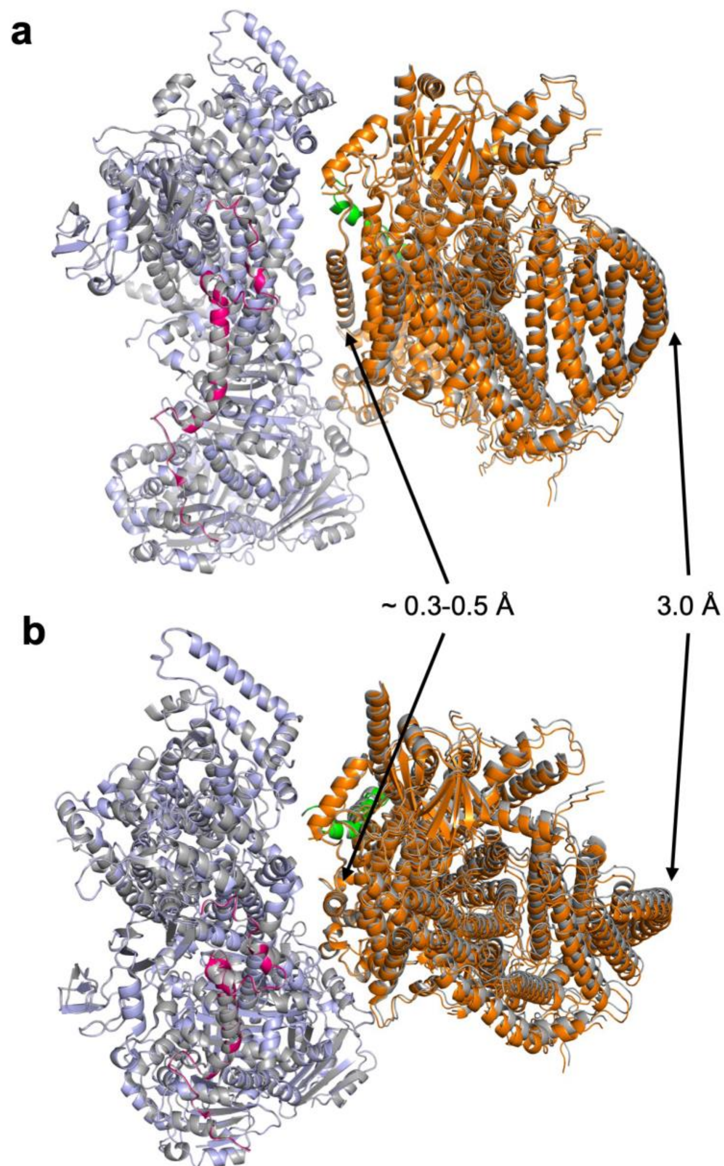

Supplementary Figure 5. Structural alignment of the two halves of the III_2IV_2 SC.

a, Side and **b**, top views of a structural alignment of the two halves of the III_2IV_2 SC, aligned on their core CIII subunits, Cor1, Cor2 and cytochrome *b*. This reveals minimal deviation of Cox5A at the SC interface (~0.3-0.5 Å), but a larger deviation of Cox13 (3.0 Å), at the extreme periphery of the SC. Cox26 and Qcr10 are displayed in green and red, respectively.

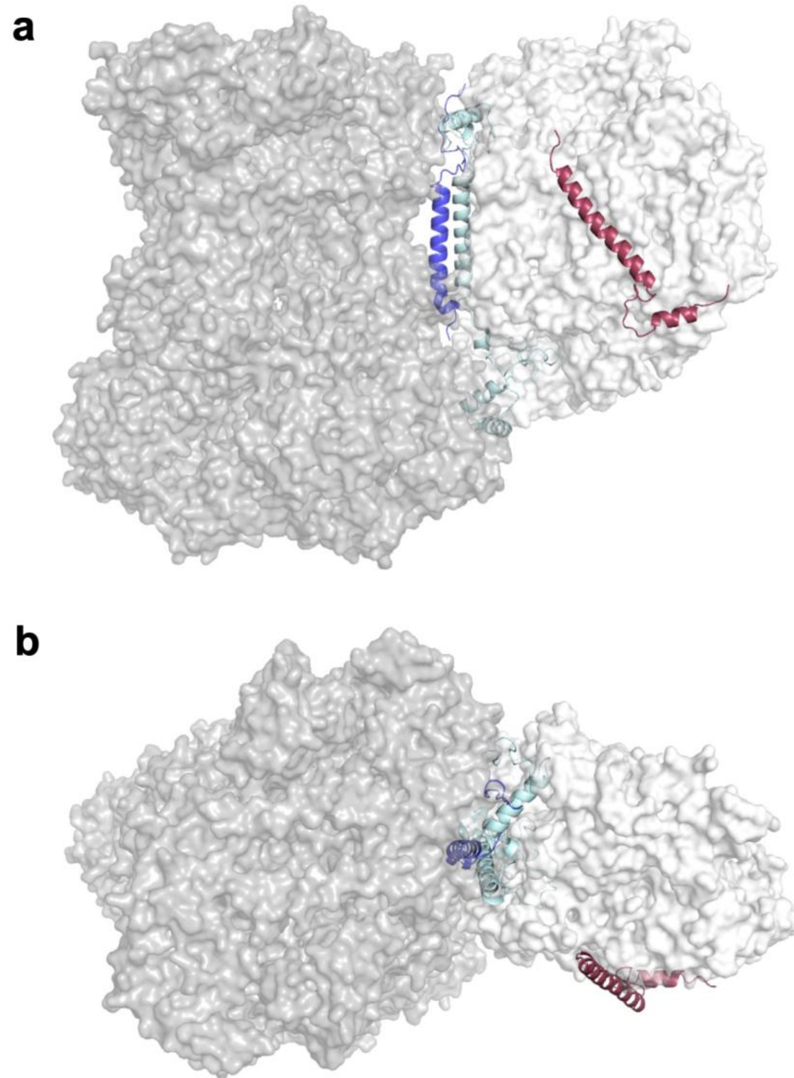

Supplementary Figure 6. Position of COX7B would not preclude interactions via COX4-1 in a mammalian CIII-CIV SC.

a, Side and **b**, top view of a putative mammalian III_2IV_1 SC formed after substitution of the yeast CIV monomer (CIVa) with bovine CIV (PDB 1V54) as per our III_2IV_2 SC structure (the other CIV is not shown). COX7B (blue), a subunit of mammalian CIV lies near COX4-1 (pale cyan; the homologue of yeast Cox5A). However, it would not interfere with any interactions between CIII and COX4-1, such as those seen in the yeast III_2IV_2 SC structure. COX7A (deep red), the subunit involved in interactions with CIII in the mammalian $I_1III_2IV_1$ respirasome is also highlighted.